




# Seismic performance of prefabricated wall panels with sliding joints for reinforced concrete frames

Chao Zhang<sup>1</sup> · Zijian Lin<sup>1</sup> · Tianhao Yu<sup>1,2</sup>  · Weiyuan Huang<sup>1,3,4</sup> · Xuesong Deng<sup>1</sup> · Zexin Lin<sup>1</sup> · Yuming Huang<sup>1</sup>

Received: 10 August 2023 / Accepted: 12 January 2024 / Published online: 6 February 2024  
© The Author(s), under exclusive licence to Springer Nature B.V. 2024

## Abstract

The seismic performance of infill wall reinforced concrete (RC) frame systems has found considerable interest in the earthquake engineering community for the last decades. However, the adverse interaction between the infills and RC frame may lead to serious collapses of the infills and casualties during earthquakes. To mitigate the adverse interaction, this study proposes an innovative damping infilled frame (DWF) system, which is mainly composed of an RC frame, prefabricated wall panels, sliding joints, and optimized connectors. The DWF system is to isolate the infills from the boundary frame and provide additional energy dissipation capacity by driving the wall panels to slide on the sliding joints. An optimized connection method is proposed to enhance the sliding mechanism and simplify the installation process. Quasi-static cyclic tests are conducted to investigate the seismic performance of the DWF system. Experimental results indicate that the DWF can effectively mitigate the detrimental infill–frame interaction, thereby exhibit stable load-bearing capacity and energy dissipation capacity loadings. Furthermore, the finite element numerical models of the DWF are established to further explore their seismic performance. Parametric analysis results reveal that both the mechanical properties of the sliding joints and the width of the infills can play crucial roles in enhancing the seismic performance of the DWF system.

---

✉ Tianhao Yu  
yutianhao@stu.scu.edu.cn

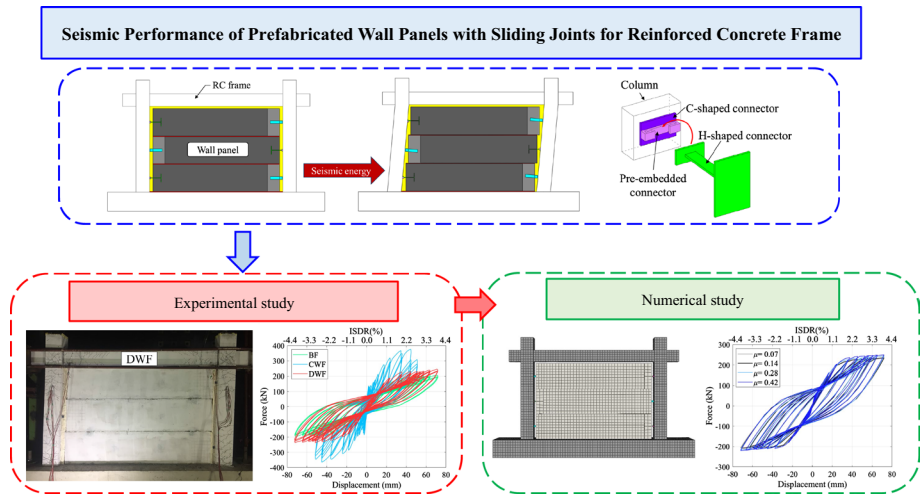
<sup>1</sup> School of Civil Engineering, Guangzhou University, 230 Wai Huan Xi Road, Guangzhou Higher Education Mega Center, Guangzhou 510006, People's Republic of China

<sup>2</sup> Department of Civil Engineering, Sichuan University, Chengdu 610065, People's Republic of China

<sup>3</sup> State Key Laboratory of Disaster Reduction in Civil Engineering, Tongji University, Shanghai 200092, People's Republic of China

<sup>4</sup> Department of Civil and Environmental Engineering, Politecnico di Milano, Milan 20133, Italy

## Graphical abstract



**Keywords** Reinforced concrete frame · Prefabricated wall panel · Innovative connection method · Sliding joint · Infill–frame interaction

## 1 Introduction

As exterior facades or partition walls, infill walls have found extensive applications within reinforced concrete frame systems, especially in constructions characterized by low to medium-rise structures (Al-Nimry et al. 2014). The infill walls tend to be considered as non-structural components and replaced by line loads in structural analysis, leading to the interactions between the infills and RC frame being ignored in structural designs. However, numerous seismic disasters and related studies have shown that the proposed interaction cannot be ignored, which may result in serious collapses of the infills and casualties during earthquakes (De Luca et al. 2018; Vasileiadis et al. 2023; Yu et al. 2023a; Pavese et al. 2017; Eren et al. 2019; Perrone et al. 2019; Sirotti et al. 2023; Furtado and de Risi 2020).

Recent investigations have mainly presented three methods to prevent the detrimental infill–frame interaction: (a) reinforcing the infills, (b) isolating the infills from the boundary frame, and (c) subdividing the infills with a sliding mechanism. The first method is to strengthen the infills locally or globally with high-performance materials, including engineered cementitious composites (Kyriakides and Billington 2014; Sharbatdar and Tajari 2021), rebar (Leeanansaksiri et al. 2018; Soltanzadeh et al. 2018; Su et al. 2023), steel stud (Bao et al. 2019), fiber-reinforced mortar (Akhoundi et al. 2018; Furtado et al. 2021; Bianchi et al. 2017), and textile-reinforced mortar (Gattesco et al. 2015). The first method can enhance the vulnerability of the infills, while the adverse infill–frame interaction cannot be prevented during high inter-story drift ratios (ISDRs) or acceleration and may even be more serious due to the over-strengthening infills (Zhang et al. 2023a; Perrone et al. 2020).

Different from the first method, the second method is to separate the infill walls from the boundary frame by setting gaps to reduce the diagonal support effect. The gaps can be infilled by some novel filling materials, such as chemical foam (Ju et al. 2012; Umar et al. 2021), elastomer layer (Mojsilovic et al. 2019), deformable blocks (Markulak et al. 2013), metal connectors (Asadzadeh et al. 2020), and stone wool (Erdem et al. 2021). This method can effectively overcome the unfavorable infill–frame interaction during in-plane shear loadings. Nevertheless, the infilled frame system lacks out-of-plane resistance capability, which may lead to the collision failure of the infills under out-of-plane loadings (Zhou et al. 2021).

To overcome the proposed problems, the third method aims to separate the infills into several subpanels, where the subpanels can slide on the sliding joints to dissipate additional energy. To ensure the sliding mechanism, the sliding friction resistance provided by the sliding joints must be much less than the shear force of the subpanels. The sliding joints tend to be made from low-shear strength materials, such as wood (Cheng et al. 2020; Preti et al. 2018), low-strength masonry mortar (Preti et al. 2012; Zhang et al. 2023b), modified asphalt waterproofs (Chen et al. 2021), styrene butadiene styrene (Su et al. 2023), high damping rubber (Zhou et al. 2021), composite elastomer (Aref and Jung 2003), friction plates (Fitzgerald et al. 2020; Mohammadi and Akrami 2010), and steel plate (Sun et al. 2018; Karadogan et al. 2019; Dal Lago et al. 2018). The proposed method can not only improve the out-of-plane capacity of the infills, but also provide the infilled frame system with additional damping. Notably, the RC columns tend to suffer shear–bending deformations actually rather than shear deformations theoretically during earthquakes (Ma and Gong 2018; Liu et al. 2011). These shear–bending deformations may lead to the plastic deformation of the connectors, which may even culminate in the corner injury of the infills and limit the sliding mechanism, especially at high ISDRs (Nie et al. 2022). For this reason, it is essential to release the vertical constraints of the infills.

This paper develops a damping infilled frame system with novel connectors to prevent the infill–frame interaction and enhance the sliding mechanism. In the subsequent sections, the working mechanism and analytical equation of the infilled frame system are developed first. Quasi-static cyclic tests are further performed to investigate the seismic performance (i.e., hysteretic responses, load-bearing capacity degradation, secant stiffness degradation, and energy dissipation behavior) of the infilled frame system. Finite element models are established to explore the effect of various sliding joints and the weight of the infills on the seismic performance of the infilled frame system.

## 2 Prefabricated wall panels with sliding joints for RC frame

### 2.1 Configuration

The DWF system is composed of an RC frame, prefabricated wall panels, sliding joints, H-shaped connectors, C-shaped connectors, T-shaped connectors, pre-embedded connectors, and flexible fillers (Fig. 1). To ensure the concrete strength and shorten the construction schedule, the RC wall panels with the H-shaped connectors are prefabricated. The sliding joints are constructed by the low-strength mortars to ensure stable low friction force during lateral loadings. The H-shaped connectors with C-shaped connectors, and T-shaped connectors are installed between the one end of the wall panels and boundary frame to drive the wall panels sliding on the damping layers and provide the wall panels with certain

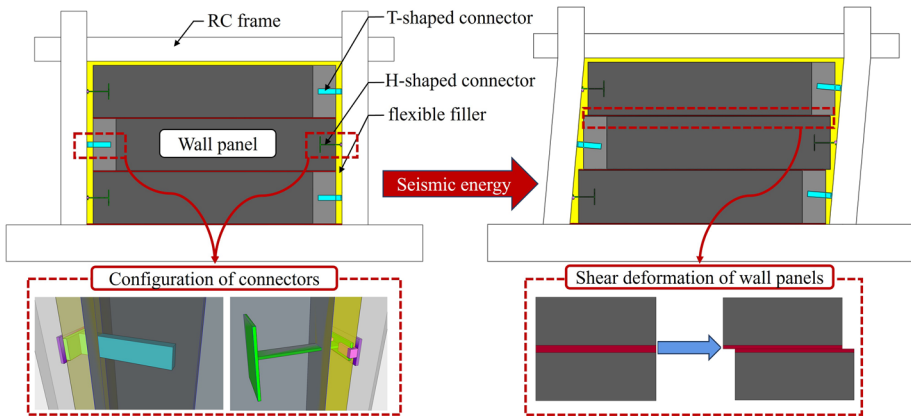


**Fig. 1** Structural schematic and deformed modes of the DWF system

out-of-plane capability (Fig. 2a). The C-shaped connectors are welded onto the pre-embedded connectors, and connected to the H-shaped connectors. To provide the wall panels with sufficient out-of-plane resistance of the infilled frame system, the T-shaped connectors are welded to the pre-embedded connector on the column and inserted into the reserved gaps on the other end of the wall panels (Fig. 2b). To mitigate the infill–frame interaction, gaps are designed to isolate the infills from the RC frame. Polyethylene foams with excellent compression properties are used to fill the gaps.

### 2.2 Working mechanism

As shown in Fig. 1, shear–bending deformations occur on the columns that drive the infills sliding on the sliding joints through the H-shaped connectors. The low-strength mortar exhibits much lower shear resistance than the lateral force of the subpanels, thereby the shear

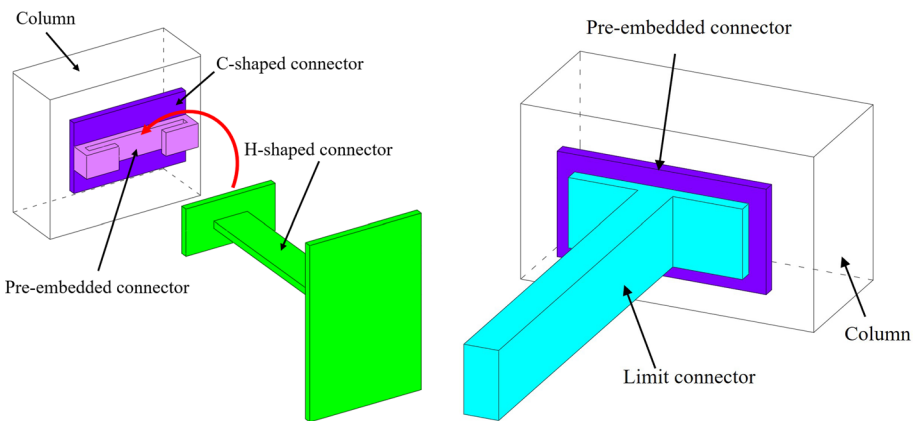


**Fig. 2** Local connection schematic: **a** H-shaped connector with C-shaped connector and **b** T-shaped connector

deformations can majorly occur on the sliding joints. Moreover, the bending deformations of columns may lead to the plastic deformations of the H-shaped connectors and limit the sliding mechanism of the wall panels. Thus, the H-shaped connectors are embedded into the C-shaped connectors to prevent the plastic deformations and release the vertical restraint of the damping wall panels. Furthermore, the wall panels can keep resilient and the sliding joints can be regarded as the damping layers to perform stable energy consumption capacity for the DWF system. Besides, the out-of-plane capacity can be oversupplied by both the H-shaped and T-shaped connectors during earthquakes. This study focuses on the working mechanism of the proposed DWF system, and the number of the subpanels involved in this study is three. Notably, according to the requirements of actual applications, the number of wall panels can be increased or decreased to set a door or window opening and other materials can be applied as the wall panels.

### 2.3 Analytical equations

The lateral load-bearing capability of the DWF system is a vital mechanical parameter to evaluate its validity of the working mechanism (Dall’Asta et al. 2017). The overall lateral force of the DWF ( $F_{DWF}$ ) is mainly contributed from the lateral force of the boundary frame ( $F_F$ ) and the total reactive force exerted on the frame by the damping wall panels ( $F_{DWF-m}$ ), which can be defined by Eq. (1). Theoretical diagram of contributions of forces for the DWF is presented in Fig. 3.

$$F_{DWF} = F_F + F_{DWF-m} \tag{1}$$

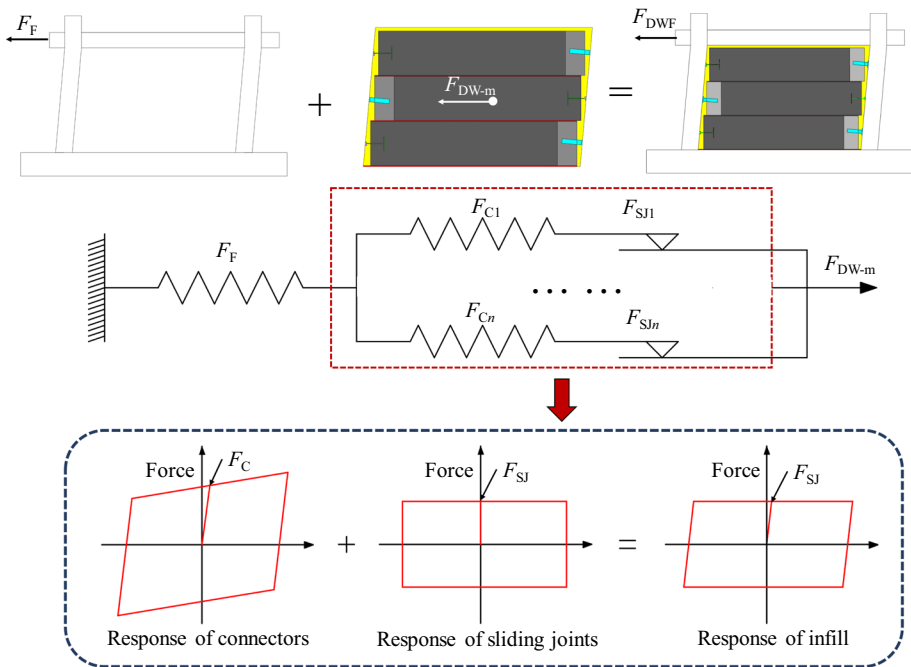


Fig. 3 Theoretical diagram of contributions of forces

The mechanical response of a piece of damping wall panel can be simplified as the steel connector in series with the wall panel, which slides on the sliding joint. Thus,  $F_{DW}$  can be obtained by:

$$F_{DW} = \begin{cases} F_C & \text{if } |F_C| \leq |F_{SJ}| \\ F_{SJ} & \text{if } |F_C| > |F_{SJ}| \end{cases} \quad (2)$$

where  $F_C$  and  $F_{SJ}$  are the lateral force of the connectors and sliding joints, respectively. The equations of  $F_C$  and  $F_{SJ}$  can be further calculated by:

$$F_C = n_C \sigma_C A_C \quad (3)$$

$$F_{SJ} = n_{SJ} \tau_{SJ} A_{SJ} \quad (4)$$

where  $n_C$  and  $n_{SJ}$  are the numbers of the connectors and sliding joints per wall panel, respectively;  $\sigma_C$  and  $A_C$  represent the strength and sectional area of the connectors, respectively;  $\tau_{SJ}$  and  $A_{SJ}$  are the shear strength and shear area of the sliding joints, respectively. The value of  $F_C$  is designed much lower than that of  $F_{SJ}$  to ensure the sliding mechanisms of the wall panels. The steel connectors without vertical restraints maintain resilience, while the additional energy dissipation capacity of the damping infills is provided by the sliding joints. It should be noted that the interaction of the infill wall to the boundary frame can be theoretically simplified as the friction force of the sliding joints to the boundary frame, while the experimental value of the DWF is lower than the theoretical one. It is reasonable that the difference value between the DWF and the bare frame could not be simply considered as the friction force of the sliding joints. A steel frame with low and stable lateral force might obtain a more accurate friction force of the sliding joints for the infilled wall system (Preti et al. 2015; Huang et al. 2023).

## 3 Experimental study

### 3.1 Specimens design

The quasi-static tests are performed to explore the seismic performance of the proposed DWF system. According to the *Code for Design of Concrete Structures* GB50010-2010 (2010), three 1:2 scaled specimens are designed and manufactured, including a bare RC frame (BF), conventional wall panels with an RC frame (CWF), and DWF. Notably, the RC frames of all specimens are designed with the same geometric dimensions and materials.

#### 3.1.1 Specimen BF

Figure 4 illustrates the geometric dimensions of specimen BF. Specimen BF has a story height of 1800 mm and a span of 2700 mm. The cross-sections of columns, beam, and girder are 250 mm × 250 mm, 160 mm × 230 mm, and 350 mm × 600 mm, respectively. The C25 concrete is used to reinforce the RC components. Note that to improve the shear resistance of the joint zones, the post-pouring areas are constructed with C40 concrete and the spacing of the stirrups is decreased. The HRB400 and HPB300 are applied as the longitudinal rebars and stirrups, respectively.

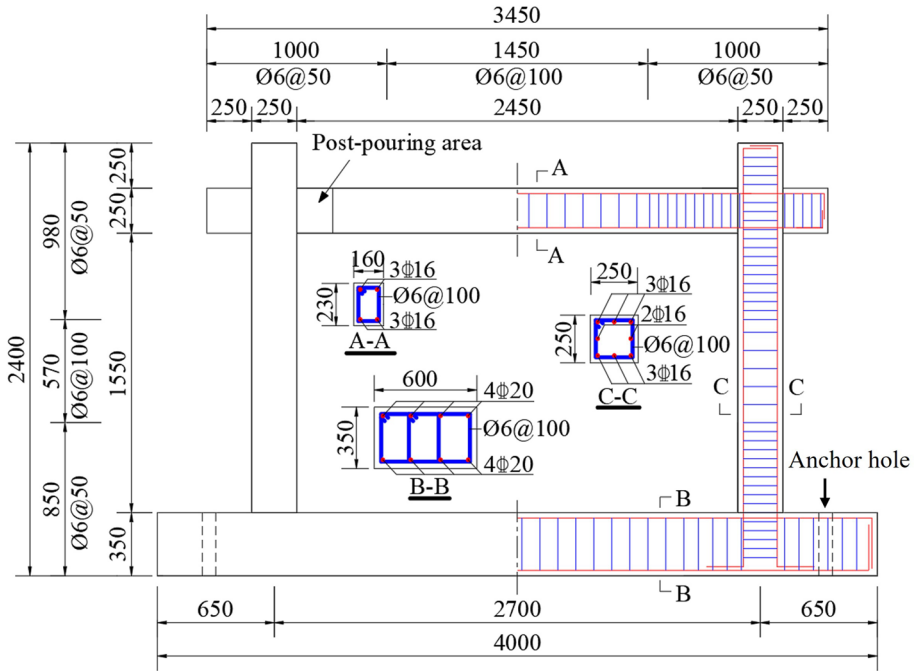


Fig. 4 Geometric configurations of specimen BF (unit: mm)

### 3.1.2 Specimen CWF

Figure 5 depicts the geometric dimensions and reinforcement details of specimen CWF. The infill wall is composed of three prefabricated subpanels. The subpanels are made from C10 concrete and reinforced with four  $\phi 8$  longitudinal rebars and six  $\phi 6$  stirrups spaced at intervals of 450 mm. To prevent the boundary frame from crashing into the wall panels, a

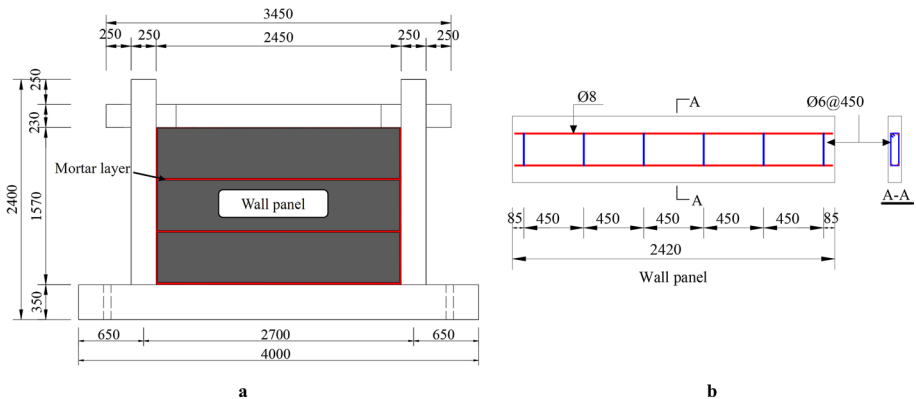
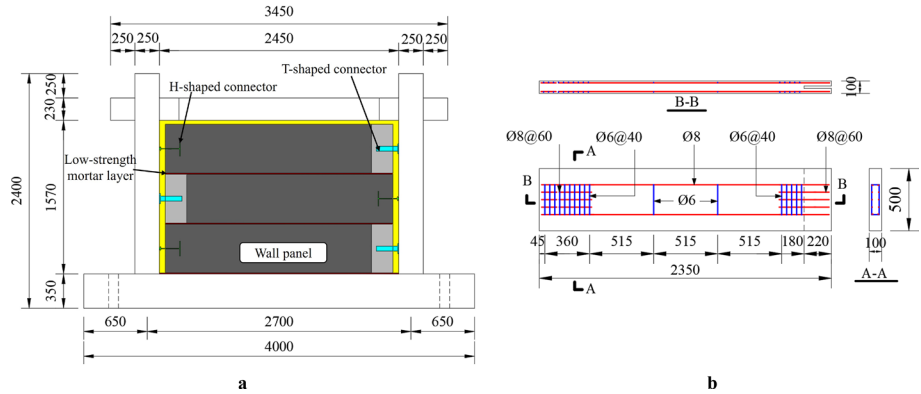
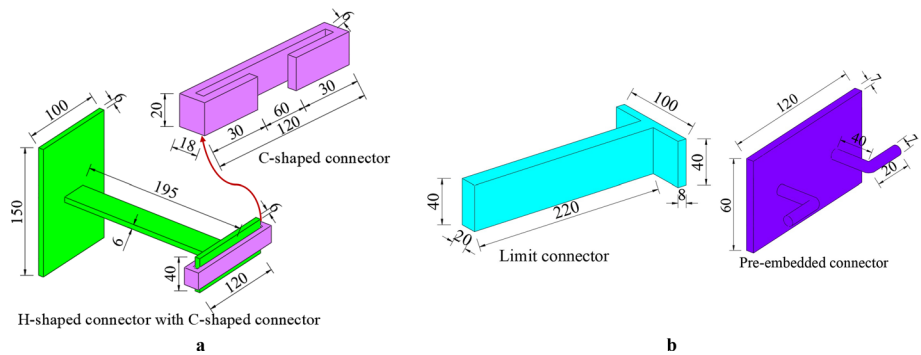


Fig. 5 Specimen CWF: **a** geometric dimensions of specimen and **b** reinforcement of conventional wall panels (unit: mm)



**Fig. 6** Specimen DWF: **a** geometric dimensions of the whole specimen and **b** reinforcement of damping wall panels (unit: mm)



**Fig. 7** Design details of **a** H-shaped connector with C-shaped connector; **b** T-shaped connector and pre-embedded connector (unit: mm)

50 mm gap is reserved between them and filled with the traditional mortar. The thickness of the traditional mortar layers between the adjacent wall panels is designed as 20 mm. Note that the experiment on CWF is designed to explore the adverse interaction of the traditional infilled frame system, so that no seismic measure is used between the subpanels and the boundary frame.

### 3.1.3 Specimen DWF

Figure 6 shows the geometric dimension of specimen DWF. The gap of 50 mm is reserved between the damping infills and the boundary frame to prevent the potential infill–frame interaction. The H-shaped connectors with C-shaped connectors link the one end of the wall panels to the frame and drive the wall panels sliding on the low-strength mortar layers. Note that to release the vertical constraints of the infills, H-shaped connectors are embedded into C-shaped connectors which are wedged to the pre-embedded connectors on the columns (Fig. 7). The other end of the wall panels has a groove with a depth of 220 mm and a width of 20 mm to cooperate with the T-shaped connectors for increasing the out-of-plane capability of the damping infills.



For improving the cyclic performance of the infill system, low-strength mortars are applied as the damping layers. The connectors are all made of Q235 steel.

The installation processes of specimen DWF are illustrated in Fig. 8. The RC frame and wall panels are prefabricated to improve the installation efficiency of the DWF system. At first, the pre-embedded connectors and C-shaped connectors are installed on the columns, and a sliding layer is installed on the bottom beam (Fig. 8a). Then, the bottom wall panel is installed on the sliding layer, the T-shaped connector is welded to the corresponding pre-embedded connectors, and the H-shaped connector is embedded into the C-shaped connector (Fig. 8b). Subsequently, the middle and top wall panels can be installed by the similar installation procedures (Fig. 8c,d). Finally, flexible material can be used to fill the gap between the damping infills and the boundary frame. Note that the optimized connectors have the advantages of enhancing the sliding mechanism by releasing the vertical constraints of the wall panels and shortening the installation process.

### 3.2 Material property

For determining the material properties of the steel rebars and connectors, three steel components are designed and tested based on the *Metallic Materials–Tensile Testing at Ambient Temperature* GB/T 228.1-2010 (1996) (Table 1). Three concrete samples are designed and tested according to the *Standard for Test Methods of Mechanical Properties of Ordinary Concrete* GB/T 50081-2016 (2003) (Table 2). Based on the *Code for Acceptance of Constructional Quality of Masonry Structures* GB 50203-2011 (2011), Tables 3 and 4 present the weight proportions and material properties of the conventional mortars and low-strength mortars.

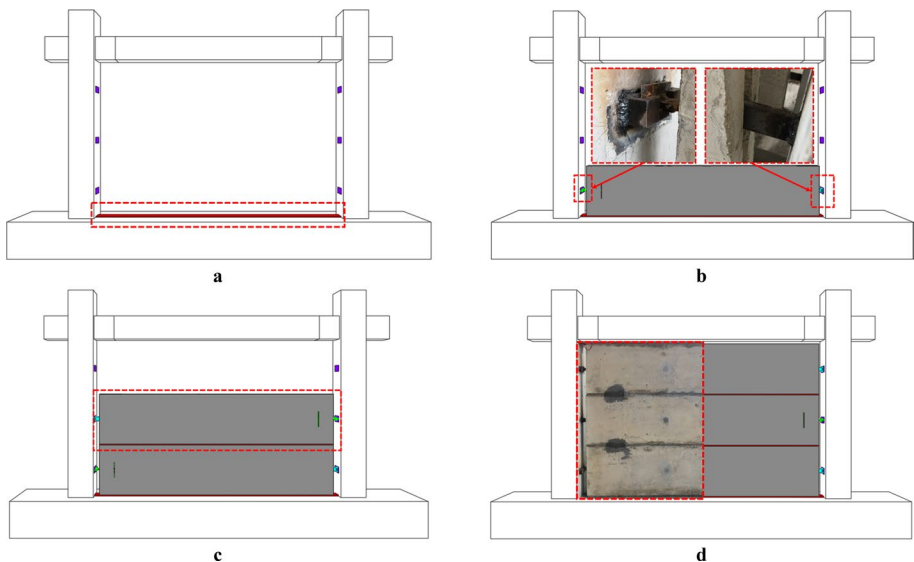


**Fig. 8** Installation processes of specimen DWF: **a** sliding joints and pre-embedded connectors, **b** bottom wall panel, **c** middle wall panel, and **d** top wall panel

**Table 1** Material properties of steel components

Steel sample	Bar diameter (mm)	Yield strength (MPa)	Ultimate tensile strength (MPa)	Modulus of elasticity (GPa)
HPB300 Rebars	6	356	428	191
HRB400 Rebars	16	408	548	194
Q235 steel plates	–	272	402	178

**Table 2** Material properties of concrete samples

Concrete strength	Compression strength (MPa)	Young's modulus (MPa)
C10	10.63	$1.99 \times 10^4$
C25	24.89	$2.93 \times 10^4$
C40	44.45	$3.45 \times 10^4$

**Table 3** Weight proportions of mortars

Mortar type	Sand	Water	Cement
Traditional mortar	4.25	0.83	1.00
Low-strength mortar	6.42	1.17	1.00

**Table 4** Material properties of mortars

Mortar type	Conventional mortar	Low-strength mortar
Compressive strength (MPa)	6.14	3.02
Shear strength (MPa)	0.24	0.15

### 3.3 Test setup

Figure 9 illustrates the layout of the test setup. The bottom beam is fixed to the strong floor by the bolts and constrained by the lifting jacks. The MTS actuator with a maximum lateral force of 3000 kN and a maximum displacement of 1000 mm is used to conduct the tests. Two lifting jacks are used to provide the columns with the axial load. The relative inter-story displacement can be detected by two linear variable displacement transducers (LVDTs).

### 3.4 Loading protocol

The axial force with 180 kN is loaded to the columns, which represents 20% of the designed axial force of the columns. The lateral loading is performed by ISDRs (the ratio of the lateral displacements to the effective height of the frame) with three cycles per

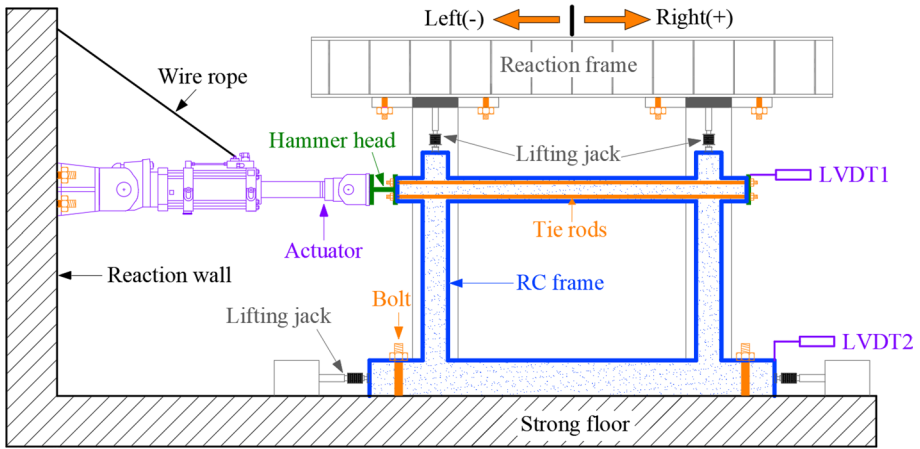


Fig. 9 Test setup

loading stage, as shown in Fig. 10. It is noted that the experiments are terminated once the lateral force of the specimens decreases to 85% of its peak force.

## 4 Experimental results

### 4.1 Experimental phenomena

#### 4.1.1 Specimen BF

Figure 11 shows the experimental phenomena of specimen BF. Several horizontal cracks occurred around the column base, and minor concrete shedding was observed at the left column foot with ISDR of 0.13%. At 1.00% ISDR, the cracks further explored and the plastic hinge regions were located at the beam-column joints. Then, with ISDR increasing to 2.86%, the cracks continued developing. Significant concrete crushing occurred at

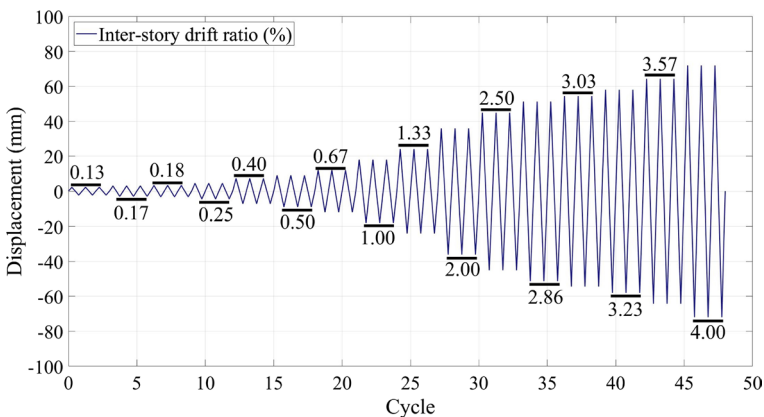
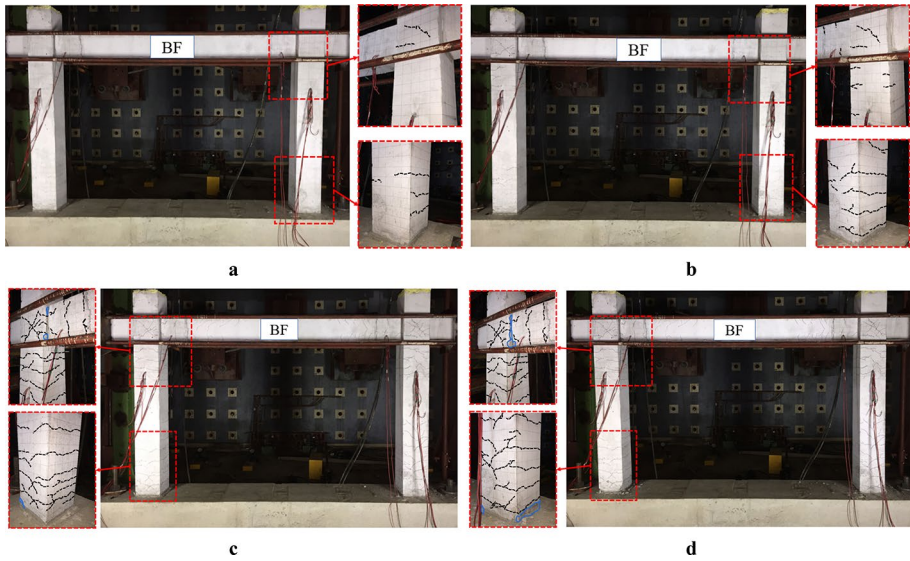


Fig. 10 Loading protocol



**Fig. 11** Failure patterns of specimen BF at ISDR of **a** 0.13%, **b** 1.00%, **c** 2.86%, and **d** 4.00%

beam-to-column joints and the column ends when ISDR achieved 4.00%. Overall, the concrete cracking is primarily concentrated near the beam-to-column joints, which is consistent with the failure modes of the traditional bare frames.

#### 4.1.2 Specimen CWF

Figure 12 plots the damage patterns of specimen CWF. As ISDR reached 0.13%, cracks occurred on the conventional mortar and wall panels due to no seismic mitigation between the infills and boundary frame. When ISDR reached 1.00%, the cracks further explored and

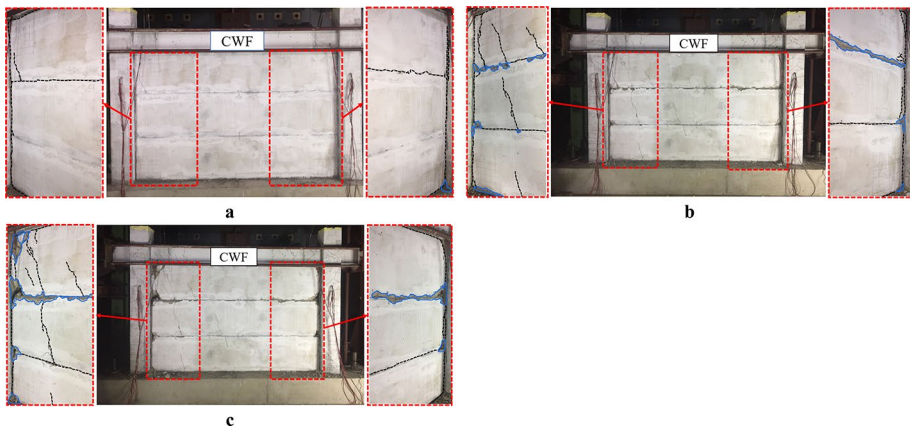


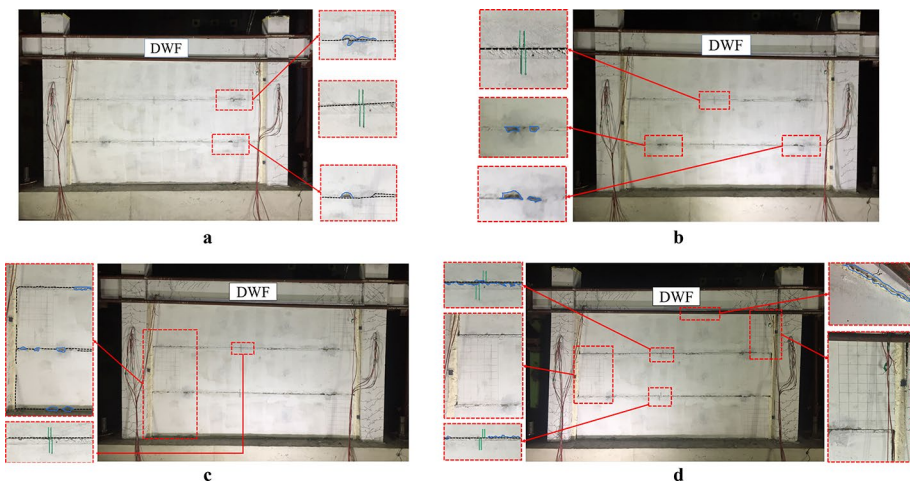
**Fig. 12** Failure patterns of specimen CWF at ISDR of **a** 0.13%, **b** 1.00%, and **c** 2.86%

the concrete of the wall panels was slightly peeled due to the detrimental infill–frame interaction. Under ISDR of 2.86%, various new cracks occurred on the wall panels, resulting in the serious corner concrete crushing of the wall panels. These confirm that the adverse infill–frame interaction may result in the spalling of the conventional mortar joints and severe concrete damage at the wall panel corners.

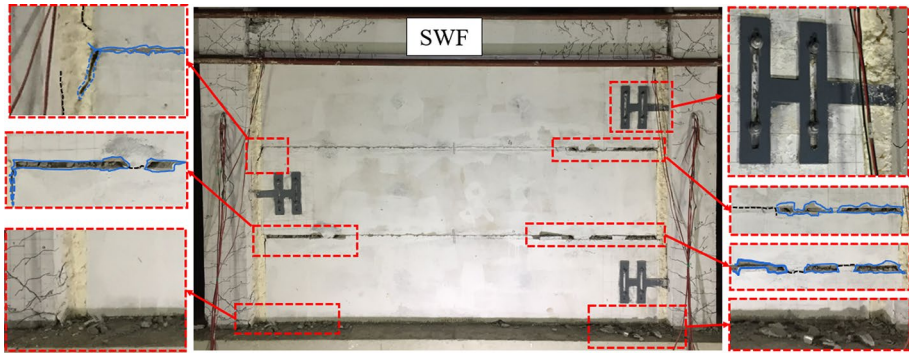
#### 4.1.3 Specimen DWF

Figure 13 illustrates the failure patterns of specimen DWF. At 0.13% ISDR, lateral cracks and slight detachment were observed on the low-strength mortar layer due to the much lower shear strength than the tensile strength of the wall panels. Furthermore, the relative displacements between adjacent wall panels were small. As ISDR increased to 1.00%, the relative maximum displacement between the middle and top wall panels reached about 5 mm. At 2.86% ISDR, the flexible layers were significantly compressed by the wall panels. Moreover, the maximum relative deformation between the top and middle wall panels achieved about 20 mm. Note that specimen DWF has similar failure modes of the RC frame to specimen BF. These indicate that the DWF system can mitigate the unfavorable infill–frame interaction and implement the expected sliding mechanism.

To further explain the advantages of the optimized connectors, the experimental results of specimen DWF are compared with a similar damping infilled frame system (SWF) in reference (Zhang et al. 2022). Figure 14 shows the failure patterns of SWF at 4.00% ISDR. Compared with specimen DWF, the failure of the sliding joints was more serious. Moreover, slight concrete crushing occurred on the wall panels corners and significant bending was observed on the straight parts of the steel connectors. These can be explained that the columns tend to suffer shear–bending deformations rather than shear deformations theoretically during earthquakes. The bending deformation driven by the steel connectors to the damping wall panels may lead to the plastic deformations of the connectors and limit the sliding mechanism of the wall panels. However, thanks to the optimized design of the connectors for specimen DWF, the embedded connection method between the H-shaped connectors and C-shaped connectors can effectively release the potential vertical



**Fig. 13** Failure patterns of specimen DWF at ISDR of **a** 0.13%, **b** 1.00%, **c** 2.86%, and **d** 4.00%



**Fig. 14** Failure patterns of SWF in literature (Zhang et al. 2022) at 4.00% ISDR

displacements of the wall panels (Fig. 2a). Therefore, the wall panels and sliding joints can be excellently protected by the optimized connection method during earthquakes.

## 4.2 Hysteretic responses

Figures 15 and 16 show the hysteretic curves and envelope curves of all specimens, respectively. Specimen CWF exhibits a significantly fuller hysteretic capacity than the other specimens owing to the adverse infill–frame interaction. Nonetheless, due to the serious crack developments of the conventional infills, the load-bearing capability of specimen CWF occurs a non-negligible decrease at ISDR of 2.50%. Notably, specimen DWF exhibits a similar hysteretic response to specimen BF benefiting from the sliding mechanism of the DWF system. Furthermore, the load-bearing capability of specimen DWF is further 4.44% higher than that of SWF on average, indicating that the optimized connectors can effectively enhance the sliding mechanism of the DWF system.

## 4.3 Load-bearing capacity degradation

The lateral load-bearing capacity degradation coefficient ( $\lambda_i$ ) is used to evaluate the load capacity stability of the specimens under cyclic loadings, which can be calculated by Eq. (5). The coefficient of variation (COV) is a commonly used index to assess the variability of  $\lambda_i$  at different ISDRs, which can be defined by Eq. (6).

$$\lambda_i = \frac{F_{i+1}}{F_i} \quad (5)$$

$$COV = \frac{\alpha}{\bar{\delta}} \times 100\% \quad (6)$$

where  $F_i$  is the peak force of the specimens at the  $i$ -th loop, and  $\bar{\delta}$  and  $\alpha$  represent the mean value and standard deviation of  $\lambda_i$ , respectively.

Figure 17 depicts  $\lambda_i$  of all specimens. The mean values of  $\lambda_1$  and  $\lambda_2$  of specimen CWF are 4.46% and 2.94% lower than those of specimen BF, while the corresponding COVs are 61.45% and 11.05% higher. It is due to the cumulative concrete damage of the conventional

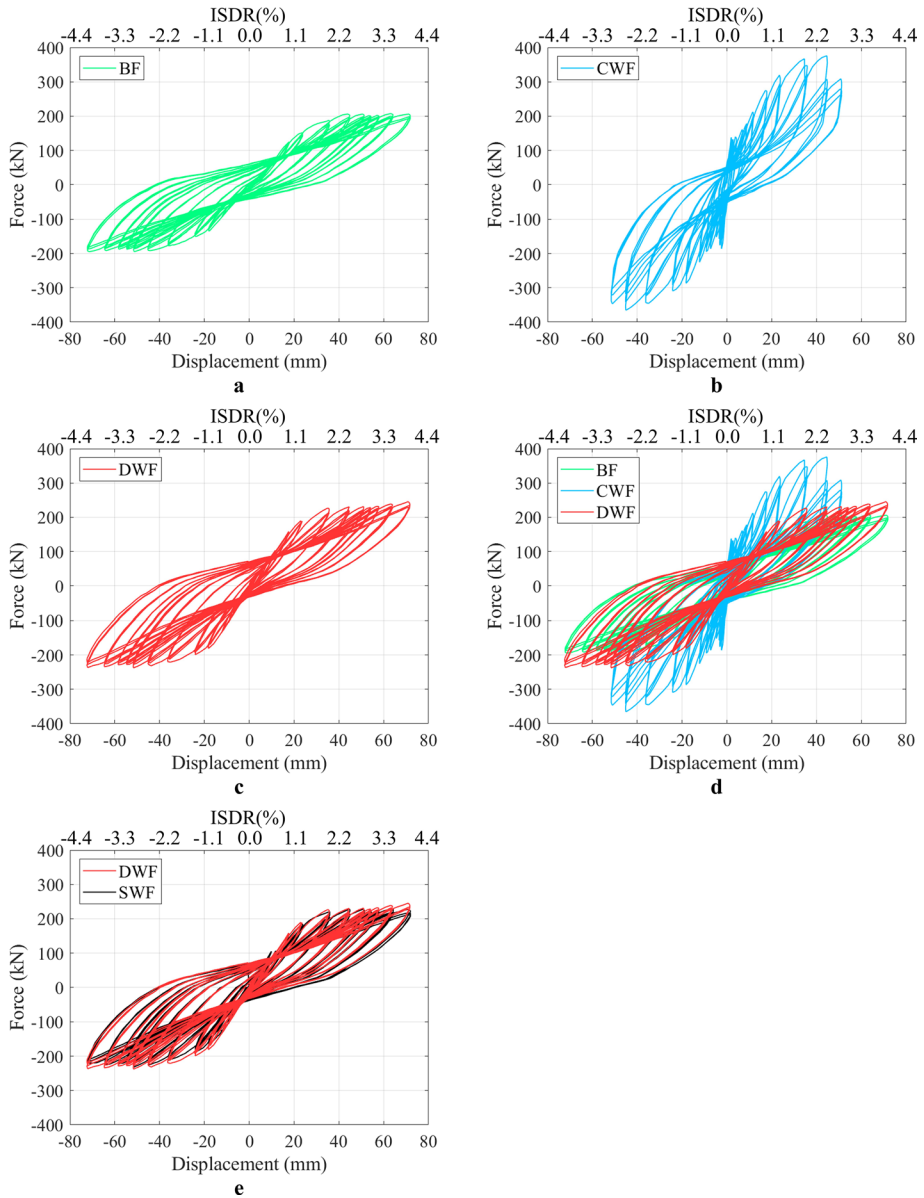


**Fig. 15** Hysteretic curves for **a** specimen BF, **b** specimen CWF, **c** specimen DWF, **d** all tested specimens, and **e** SWF (Zhang et al. 2022)

infill panels. On the contrary, specimen DWF with the slight injury of the wall panels can exhibit a similar load-bearing capacity degradation to specimen BF. It shows that the separation mechanism of the infills from the boundary frame for the DWF system can effectively protect the damping wall panels from severe damage. Compared with specimen SWF, the higher values of  $\lambda_i$  and lower COVs confirm that specimen DWF can perform

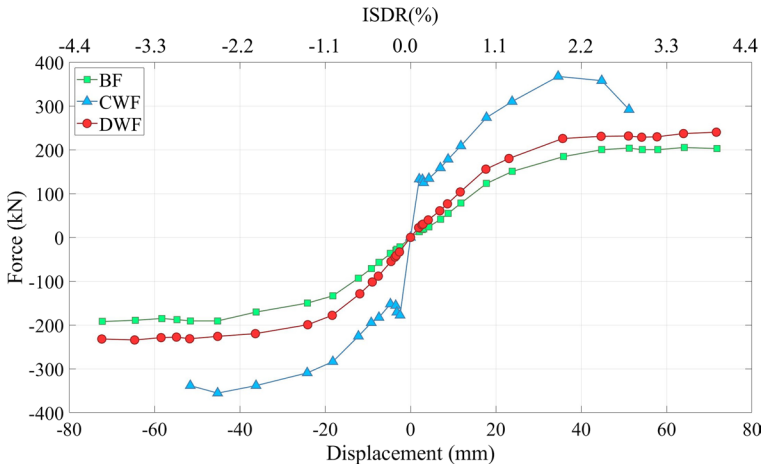


Fig. 16 Enveloped curves of specimens

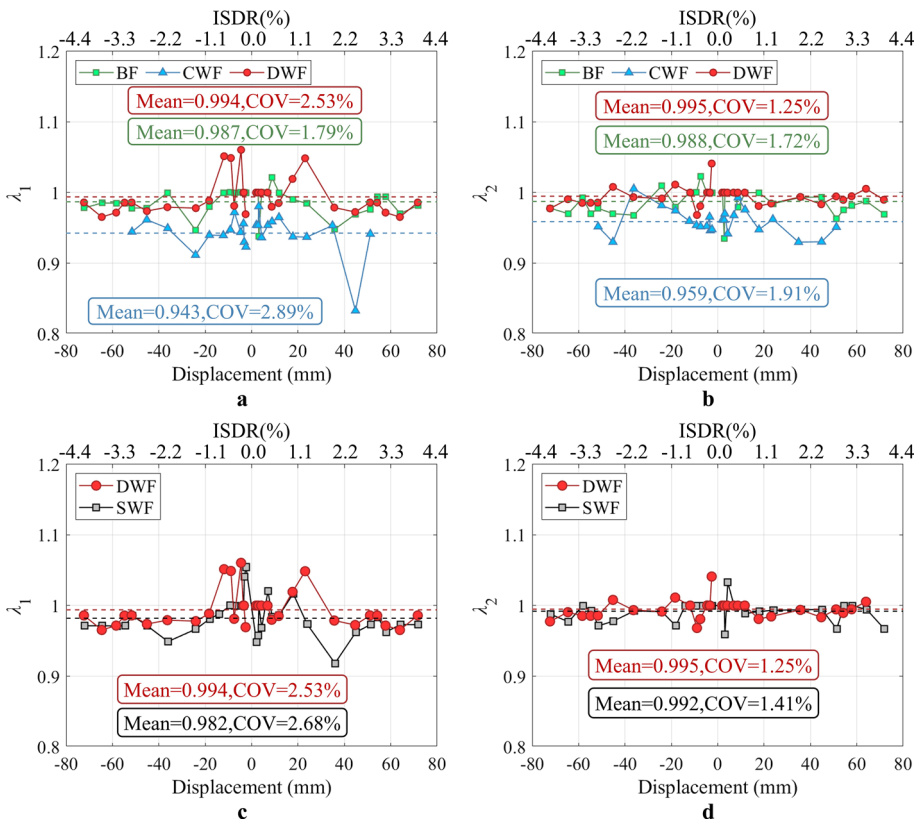


Fig. 17 Degradation coefficient of the lateral load-bearing capacity of a  $\lambda_1$  and b  $\lambda_2$  for all tested specimens; c  $\lambda_1$  and d  $\lambda_2$  for SWF (Zhang et al. 2022)



better loading capacity stability benefitting from the effective preventions of the damping wall panels and mortar layers.

### 4.4 Secant stiffness degradation

The secant stiffness of specimens is used to evaluate the effective stiffness capacity of the specimens under different ISDRs, which can be defined by:

$$K_i = \frac{F_i}{X_i} \tag{7}$$

where  $K_i$ ,  $F_i$ , and  $X_i$  are the secant stiffness, maximum force, and lateral displacement of the specimens at the  $i$ -th cycle, respectively.

Figure 18a presents the secant stiffness degradation curves of all specimens. Thanks to the overlarge support between the conventional infills and the boundary frame, specimen CWF exhibits initial stiffness 9.16 times higher initial stiffness than specimen BF. Subsequently, the secant stiffness of specimen CWF rapidly decreases due to the serious concrete failure of the conventional infills. However, the initial stiffness and average stiffness of specimen DWF are only 58.40% and 39.39% higher than those of specimen BF, respectively. It indicates that the adverse stiffness degradation in the scant stiffness of the infills can be significantly enhanced by reserving the gaps between the infills and the boundary frame. Moreover, the average stiffness of specimen DWF is slightly higher than that of specimen SWF during the whole loading procedure. It is reasonable that the optimized connection method can further prevent the sliding layers and damping infill panels, so the infills can exhibit stable stiffness capability.

### 4.5 Energy dissipation capability

The equivalent viscous damping ratios ( $\xi_{eqv}$ ) are used to assess the effective damping capability of the specimens under various ISDRs, which can be calculated by:

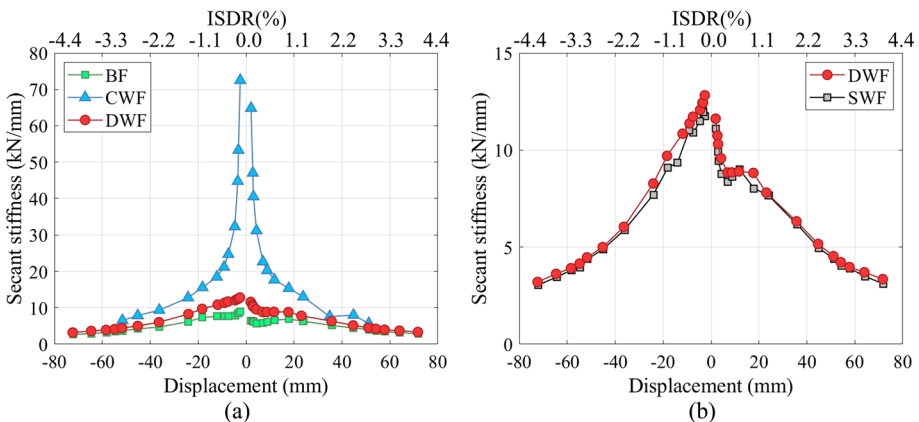


Fig. 18 Secant stiffness degradation curves for a all tested specimens and b SWF (Zhang et al. 2022)

$$\xi_{eqv} = \frac{E_{loop}}{2\pi E_{sto}} \tag{8}$$

where  $E_{loop}$  and  $E_{sto}$  represent the energy dissipation area enclosed by each hysteretic loop and the stored energy at the specific loading displacement, respectively.

Figure 19 shows the comparison of  $\xi_{eqv}$  for all specimens. The  $\xi_{eqv}$  of specimen CWF is much higher than that of specimen BF at small ISDR due to the overlarge diagonal support between the conventional infills and the boundary frame. Nevertheless, benefitting from the severe concrete cracking developments caused by the infill–frame interaction,  $\xi_{eqv}$  of specimen CWF rapidly decreases. On the contrary, thanks to the low injury of the damping infills,  $\xi_{eqv}$  of specimen DWF has a similar trend to that of specimen BF. Thanks to the additional sliding working mechanism, specimen DWF exhibits  $\xi_{eqv}$  10.11% higher than specimen BF on average. These indicate that the DWF system exhibits similar energy dissipation capability to the bare frame through mitigating the adverse interaction. Moreover,  $\xi_{eqv}$  of specimen DWF is 6.65% higher than that of specimen SWF. It is reasonable that thanks to the vertical constraints decoupling function provided by the optimized connectors, the DWF system with lower damage sliding layers can perform more stable energy dissipation capability.

## 5 Numerical study

### 5.1 Modeling strategies

The finite element numerical model of the DWF system is established by the ABAQUS to further investigate its seismic performance with various sliding joints and weight of the wall panels, as shown in Fig. 20. The concrete and steel members are modeled by the eight-node solid element with reduced integration and hourglass control (C3D8R element) (Nascimbene 2022), and the rebars are modeled by the truss element (T3D2 element). The material properties of the steel and concrete parts are defined by the Steel02 and Concrete02 models, respectively. To save the calculation costs of the model, the T-shaped connectors are embedded into the C-shaped connectors, which are tied to the columns. The

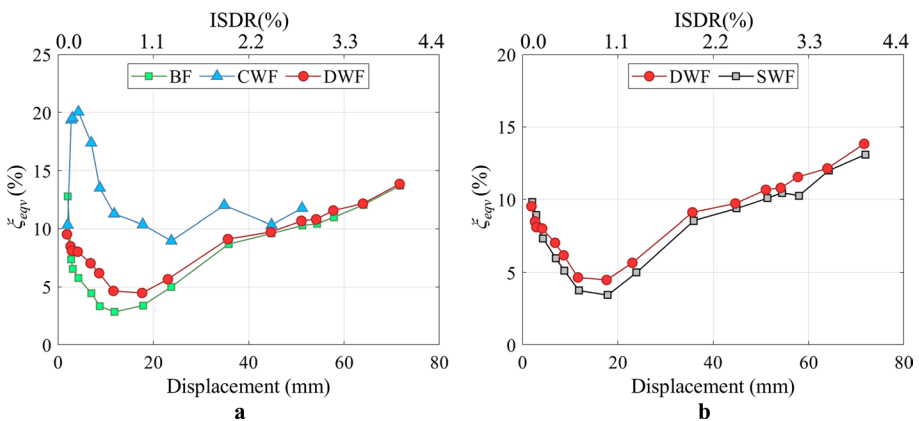
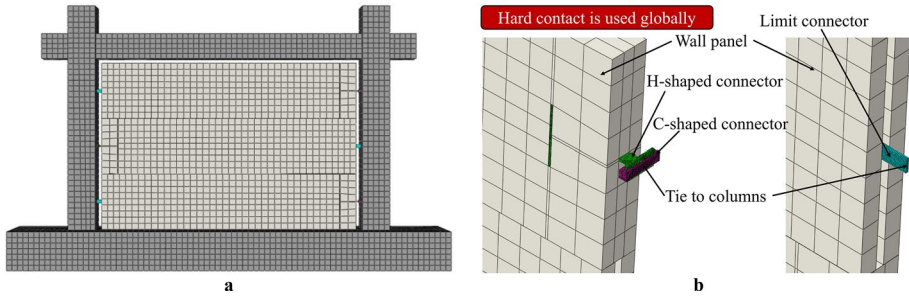


Fig. 19 Energy dissipation capability of a all tested specimens and b SWF (Zhang et al. 2022)



**Fig. 20** Finite element numerical model: **a** model DWF and **b** interaction details of connectors

rebars are embedded into the frame and wall panels. The sliding joints are simplified by being inserted into the wall panels with a friction coefficient ( $\mu$ ) of 0.14 (Eq. (9)) (Zhang et al. 2022). The hard contact interaction is used among the columns, wall panels, and connectors. The lateral displacements, which are the same as the experimental loading protocols, are applied to the left end of the top beam through a simulated reference point. The bottom beam is fully restrained.

$$\mu = \frac{F_{SJ}}{G_{DW}} \tag{9}$$

where  $G_{DW}$  is the gravity of the damping wall panels.

Figure 21 shows the experimental and numerical hysteresis curves of the DWF. It should be noted that the unloading stiffness of the model is slightly lower than that of the experiments because it is difficult for numerical simulations to show the defects caused by the elastoplastic or plastic deformations of the RC frame. However, the defects have little effect on the simulated hysteresis cycles, where good agreements of loading capacity are observed between the experimental and numerical results of the DWF. Furthermore, the deformation modes and concrete stress concentrations of the numerical model can accurately match those of the

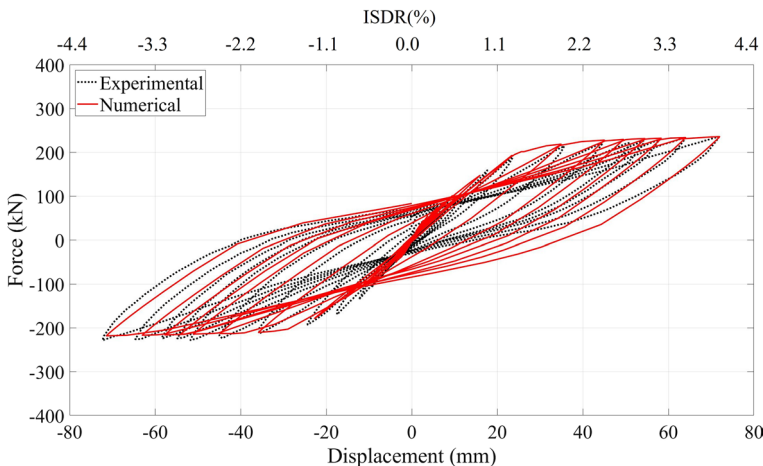


**Fig. 21** Experimental and numerical hysteresis curves of DWF

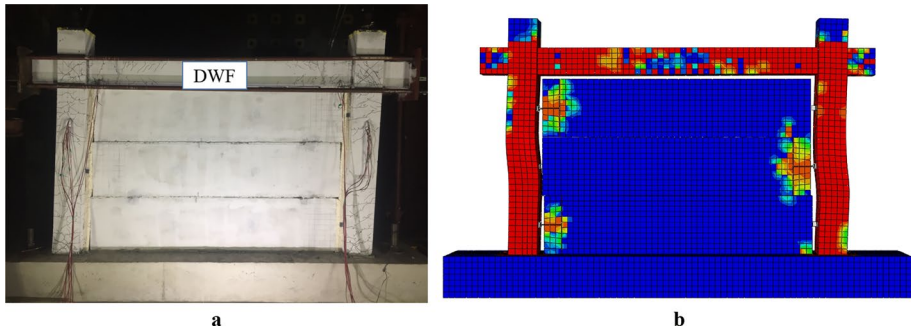


**Fig. 22** Failure modes of DWF: **a** experimental and **b** numerical at 4.00% ISDR

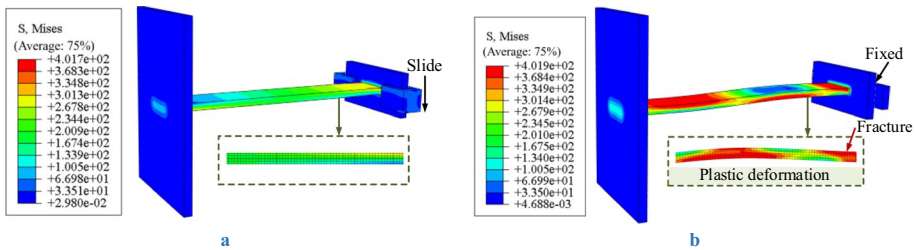


**Fig. 23** Stress distributions of H-shaped connectors **a** without and **b** with vertical restraints for top wall panel at 4.00% ISDR

experimental results (Fig. 22). These demonstrate that the developed finite element numerical model can accurately simulate the mechanical properties of the DWF system.

To validate the superiority of the optimized connectors by releasing their vertical restraints, the DWF with welded (the H-shaped connector is directly tied to the column) connectors is established, where the H-shaped connectors are directly tied to the C-shaped connectors. Figure 23 illustrates the stress distributions of the top H-shaped and C-shaped connectors for the top wall panel. Stress distributions and significant bending deformations of the connector with vertical restraints are concentrated in its straight section. It can be explained that the connector exhibits plastic deformation with the bending deformation of the column due to the vertical restraints in the connector. The continuous cumulative plasticity may lead to the fracture of the connector, especially with the increase of displacement and loading cycles (Wang et al. 2021; Yu et al. 2023b). Nevertheless, no significant localized stress concentration occurs on the connector without vertical restraints. It further validates that the optimized connectors can prevent the stress concentration in the connectors when the wall panels slide on the sliding joints.

## 5.2 Parametric study

### 5.2.1 Influence of sliding joints

Figure 24 depicts the influence of the seismic performance of the models with sliding joints. Various mechanical properties of sliding joints are simplified by setting the interaction between the adjacent wall panels different  $\mu$  (Eq. (9)). As the friction factor  $\mu$

increases from 0.07 to 0.42, the peak loading, yield loading, and initial stiffness of the models improve by 7.09%, 4.22%, and 33.31%, respectively. These reveal that the mechanical properties of sliding joints, which can be also constructed by other damping materials (Aloisio et al. 2022; Zhou et al. 2023), can play a crucial role in improving the seismic performance of the DWF system.

### 5.2.2 Influence of the width of wall panels

The models with various widths of wall panels, ranging from 50 to 300 mm, are constructed to investigate the effect of the seismic behavior of the DWF system. As shown in Fig. 25, the peak load, yield load, and initial stiffness of the model for the wall panels with a width of 300 mm are 7.52%, 4.05%, and 34.36% higher than those of the model with 50 mm, respectively. These are reasonable that the width of the damping infills can improve the shear area of the sliding joints (Eq. (4)), thus effectively enhance the seismic performance of the DWF system.

## 6 Conclusion

This paper presents the working mechanism of a novel DWF system to mitigate the adverse interaction between the infills and boundary frame. An optimized connection method is developed to avoid the plastic deformations of the steel connectors and enhance the cyclic responses of the DWF system. The experimental study is conducted to explore the seismic performance of the DWF system. The finite element models of the DWF system are established and validated based on the experimental results. Subsequently, parametric analysis is performed to explore the effect of the seismic performance of the DWF system with different sliding joints and widths of the wall panels. The major conclusions can be summarized as follows:

- (1) Obvious cracks were observed on the common infills due to the detrimental infill–frame interaction between the infills and the boundary frame. Nevertheless, thanks to the separation of the infills from the boundary frame through the reserve gaps, the damp-

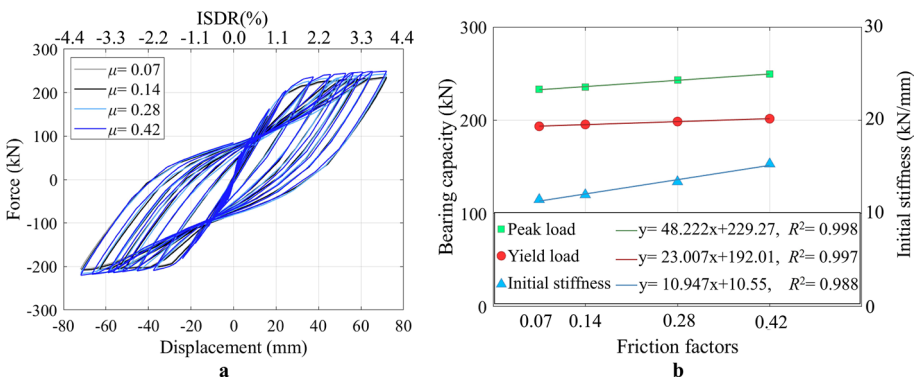


**Fig. 24** Influence of the models with different sliding joints: **a** hysteretic curves; **b** bearing capacity and initial stiffness

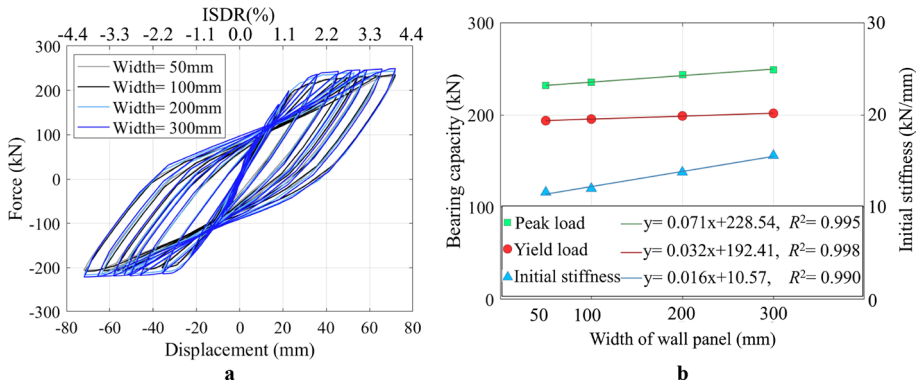


**Fig. 25** Influence of model DWF with different weight factors: **a** hysteretic curves; **b** bearing capacity and initial stiffness

ing wall panels with ignorable injuries can slide on the sliding joints even at the 4.00% drift ratio.

- (2) Benefitting from the proposed sliding mechanism, the DWF system can exhibit stable hysteretic responses, load-bearing capacity, stiffness, and energy dissipation capability, which are higher than those of the bare RC frame.
- (3) Thanks to the optimized connection method, the sliding layers and damping infills of the DWF system can be effectively prevented compared with those of the damping infilled system with traditional connectors. Therefore, the DWF system can exhibit more better hysteresis responses, stiffness properties, and damping capability.
- (4) The developed finite element numerical model can accurately predict the seismic performance of the DWF system and validate the effectiveness of the optimized connectors. The mechanical properties of the sliding joints and the width of the wall panels can significantly affect the hysteresis responses of the DWF system.

**Acknowledgements** The authors wish to gratefully acknowledge the generous support of this work by the National Natural Science Foundation of China (No. 52378498), the National Natural Science Foundation of China (No. 51508117).

**Author contributions** C.Z.: Conceptualization, Methodology, Funding acquisition, Validation, Resource. Z.L.: Investigation, Software, Writing—original draft, Data curation. T.Y.: Methodology, Supervision, Writing—original draft, Writing—review and editing. W.H.: Methodology, Supervision, Writing—review and editing. X.D.: Project administration, Resource. Z.L.: Investigation, Validation, Data curation. Y.H.: Data curation.

**Funding** The authors wish to gratefully acknowledge the generous support of this work by the National Natural Science Foundation of China (No. 52378498), the National Natural Science Foundation of China (No. 51508117).

#### Declarations

The authors declare that they have no known competing financial interests or personal relationships that could have appeared to influence the work reported in this paper.

## References

- Akhoundi F, Vasconcelos G, Lourenco P, Silva LM, Cunha F, Figueiro R (2018) In-plane behavior of cavity masonry infills and strengthening with textile reinforced mortar. *Eng Struct* 156:145–160
- Al-Nimry H, Resheidat M, Al-Jamal M (2014) Ambient vibration testing of low and medium rise infilled RC frame buildings in Jordan. *Soil Dyn Earthq Eng* 59:21–29
- Aloisio A, Boggian F, Tomasi R (2022) Design of a novel seismic retrofitting system for RC structures based on asymmetric friction connections and CLT panels. *Eng Struct* 254:113807
- Aref AJ, Jung WY (2003) Energy-dissipating polymer matrix composite-infill wall system for seismic retrofitting. *J Struct Eng Asce* 129:440–448
- Asadzadeh SA, Mohammadi M, Attari NKA, Zareei SA (2020) An experimental study on the effect of frame-to-wall connection type on the seismic behavior of steel frames infilled with autoclave-cured aerated concrete blocks. *Adv Struct Eng* 23:642–656
- Bao W, Jiang J, Shao Y, Liu Y (2019) Experimental study of the lateral performance of a steel stud wall with a semi-rigid connected frame. *Eng Struct* 183:677–689
- Bianchi F, Nascimbene R, Pavese A (2017) Experimental vs. numerical simulations: Seismic response of a half scale three-storey infilled RC building strengthened using FRP retrofit. *Open Civil Eng J* 11:1158–1169
- Chen Z, Zhou Y, Zhong G, Lu Y, Shi F (2021) Study on the cyclic shear behavior of damping layer joint for the infilled masonry wall. *Constr Build Mater* 273:121772
- Cheng X, Zou Z, Zhu Z, Zhai S, Yuan S et al (2020) A new construction technology suitable for frame partitioned infill walls with sliding nodes and large openings: test results. *Constr Build Mater* 258:119644
- Dal Lago B, Biondini F, Toniolo G (2018) Experimental investigation on steel w-shaped folded plate dissipative connectors for horizontal precast concrete cladding panels. *J Earthquake Eng* 22:778–800
- Dall'Asta A, Leoni G, Morelli F, Salvatore W, Zona A (2017) An innovative seismic-resistant steel frame with reinforced concrete infill walls. *Eng Struct* 141:144–158
- De Luca F, Woods GED, Galasso C, D'Ayala D (2018) RC infilled building performance against the evidence of the 2016 EEFIT Central Italy post-earthquake reconnaissance mission: empirical fragilities and comparison with the FAST method. *Bull Earthq Eng* 16:2943–2969
- Erdem MM, Emsen E, Bikce M (2021) Experimental and numerical investigation of new flexible connection elements between infill walls-RC frames. *Constr Build Mater* 296:123605
- Eren N, Brunesi E, Nascimbene R (2019) Influence of masonry infills on the progressive collapse resistance of reinforced concrete framed buildings. *Eng Struct* 178:375–394
- Fitzgerald D, Miller TH, Sinha A, Nairn JA (2020) Cross-laminated timber rocking walls with slip-friction connections. *Eng Struct* 220:110973
- Furtado A, de Risi MT (2020) Recent findings and open issues concerning the seismic behaviour of masonry infill walls in RC buildings. *Adv Civil Eng* 2020:9261716
- Furtado A, Rodrigues H, Arede A (2021) Experimental and numerical assessment of confined infill walls with openings and textile-reinforced mortar. *Soil Dyn Earthq Eng* 151:106960
- Gattesco N, Boem I, Dudine A (2015) Diagonal compression tests on masonry walls strengthened with a GFRP mesh reinforced mortar coating. *Bull Earthq Eng* 13:1703–1726
- Huang W, Chen Q, Zhang C, Wongso S, Zhang S et al (2023) Influence of window opening on cyclic behavior of precast infill wall with sliding joints. *Bull Earthq Eng*. <https://doi.org/10.1007/s10518-10023-01817-10515>
- Ju R-S, Lee H-J, Chen C-C, Tao C-C (2012) Experimental study on separating reinforced concrete infill walls from steel moment frames. *J Constr Steel Res* 71:119–128
- Karadogan F, Yuksel E, Khajehdehi A, Ozkaynak H, Gullu A, Senol E (2019) Cyclic behavior of reinforced concrete cladding panels connected with energy dissipative steel cushions. *Eng Struct* 189:423–439
- Kyriakides MA, Billington SL (2014) Cyclic response of nonductile reinforced concrete frames with unreinforced masonry infills retrofitted with engineered cementitious composites. *J Struct Eng* 140:04013046
- Leeanansaksiri A, Panyakapo P, Ruangrassamee A (2018) Seismic capacity of masonry infilled RC frame strengthening with expanded metal ferrocement. *Eng Struct* 159:110–127
- Liu C, Shi W, Zhao S, Pan Y (2011) Study on destructive modes of RC frame columns in Wenchuan earthquake. *Build Struct* 250–253:1224–1227
- Ma Y, Gong J-x (2018) Seismic failure modes and deformation capacity of reinforced concrete columns under cyclic loads. *Period Polytechn Civil Eng* 62:80–91

- Markulak D, Radic I, Sigmund V (2013) Cyclic testing of single bay steel frames with various types of masonry infill. *Eng Struct* 51:267–277
- Mohammadi M, Akrami V (2010) An engineered infilled frame: behavior and calibration. *J Constr Steel Res* 66:842–849
- Mojsilovic N, Petrovic M, Stojadinovic B (2019) Multi-layer masonry bed joint subjected to shear: analytical modelling. *Constr Build Mater* 205:602–610
- Nascimbene R (2022) Penalty partial reduced selective integration: a new method to solve locking phenomena in thin shell steel and concrete structures. *Curved and Layer. Struct* 9:352–364
- Nie GB, Zhang CX, Wang ZY, Xu WD, Shi YJ (2022) Shaking table test of space double-layer cylindrical reticulated shell with three-dimensional isolation bearing. *J Constr Steel Res* 189:107107
- Pavese A, Lanese I, Nascimbene R (2017) Seismic vulnerability assessment of an infilled reinforced concrete frame structure designed for gravity loads. *J Earthq Eng* 21:267–289
- Perrone D, Calvi PM, Nascimbene R, Fischer EC, Magliulo G (2019) Seismic performance of non-structural elements during the 2016 Central Italy earthquake. *Bull Earthq Eng* 17:5655–5677
- Perrone D, Brunesi E, Filiatrault A, Nascimbene R (2020) Probabilistic estimation of floor response spectra in masonry infilled reinforced concrete building portfolio. *Eng Struct* 202:109842
- Preti M, Bettini N, Plizzari G (2012) Infill walls with sliding joints to limit infill-frame seismic interaction: large-scale experimental test. *J Earthq Eng* 16:125–141
- Preti M, Migliorati L, Giuriani E (2015) Experimental testing of engineered masonry infill walls for post-earthquake structural damage control. *Bull Earthq Eng* 13:2029–2049
- Preti M, Neffati M, Bolis V (2018) Earthen masonry infill walls: Use of wooden boards as sliding joints for seismic resistance. *Constr Build Mater* 184:100–110
- Sharbatdar MK, Tajari A (2021) Experimental in-plane seismic strengthening of masonry infilled reinforced concrete frames by engineered cementitious composites (ECC). *Constr Build Mater* 293:123529
- Sirotti S, Aloisio A, Pellicciari M, Briseghella B (2023) Empirical formulation for the estimate of the equivalent viscous damping of infilled RC frames. *Eng Struct* 288:116196
- Soltanzadeh G, Bin Osman H, Vafaei M, Vahed YK (2018) Seismic retrofit of masonry wall infilled RC frames through external post-tensioning. *Bull Earthq Eng* 16:1487–1510
- Standard of China (1996) *Metallic materials-tensile testing at ambient temperature*. China Construction Industry Press, Beijing
- Standard of China (2003) *Standard for test methods of mechanical properties of ordinary concrete*. China construction Industry Press, Beijing
- Standard of China (2010) *Code for design of concrete structures*. China Architectural & Building Press, Beijing
- Standard of China (2011) *Code for acceptance of constructional quality of masonry structures*. China Architectural and Building Press, Beijing
- Su Q, Cai G, Hani M, Larbi AS, Tsavdaridis KD (2023) Damage control of the masonry infills in RC frames under cyclic loads: a full-scale test study and numerical analyses. *Bull Earthq Eng* 21:1017–1045
- Sun G, Gu Q, Li Q, Fang Y (2018) Experimental and numerical study on the hysteretic behavior of composite partially restrained steel frame-reinforced concrete infill walls with vertical slits. *Bull Earthq Eng* 16:1245–1272
- Umar Z, Shah SAA, Bibi T, Shahzada K, Ahmad A (2021) Innovative seismic isolation of masonry infills using cellular material at the interface with the surrounding RC frame. *J Build Eng* 40:102736
- Vasileiadis V, Kostinakis K, Athanatopoulou A (2023) Story-wise assessment of seismic behavior and fragility analysis of R/C frames considering the effect of masonry infills. *Soil Dyn Earthq Eng* 165:107714
- Wang B, Nishiyama M, Zhu S, Tani M, Jiang H (2021) Development of novel self-centering steel coupling beams without beam elongation for earthquake resilience. *Eng Struct* 232:111827
- Yu T, Zhang C, Niu X, Zhuang R (2023a) Seismic resilience of structures research: a bibliometric analysis and state-of-the-art review. *Earthq Struct* 25:369–383
- Yu T, Zhang C, Huang Z, Huang W, Wang S, Zhong G, Ou D (2023b) Experimental and numerical studies of a novel three-dimensional isolation device incorporating disc springs with U-shaped dampers. *Soil Dyn Earthq Eng* 174:108164
- Zhang C, Yu T, Chen Z, Huang W, Zhang S et al (2022) Seismic behavior of novel low-damage precast infill walls with sliding joints for reinforced concrete frame. *Earthquake Eng Struct Dynam* 51:3730–3754
- Zhang C, Wongso S, Wang H, Huang W, Shi F et al (2023a) Seismic responses of infill walls with sliding joints and openings in semi-rigid steel frame. *J Build Eng* 63:105457



- Zhang C, Yang Z, Yu T, Huang W, Deng X et al (2023b) Experimental and numerical studies of improving cyclic behavior of infilled reinforced concrete frame by prefabricated wall panels with sliding joints. *J Build Eng* 77:107524
- Zhou Y, Chen Z, Zhong G, Lu Y, Zhang C, Li D (2021) Experimental study on out-of-plane behaviour of an infilled masonry wall with damping layer joint. *Eng Struct* 246:112993
- Zhou Y, Chen Z, Zhong G (2023) Investigation on the seismic performance of the masonry infill wall with damping layer joint. *Eng Struct* 285:115979

**Publisher's Note** Springer Nature remains neutral with regard to jurisdictional claims in published maps and institutional affiliations.

Springer Nature or its licensor (e.g. a society or other partner) holds exclusive rights to this article under a publishing agreement with the author(s) or other rightsholder(s); author self-archiving of the accepted manuscript version of this article is solely governed by the terms of such publishing agreement and applicable law.